Modeling of Fatigue Crack Induced Nonlinear Ultrasonics Using a Highly Parallelized Explicit Local Interaction Simulation Approach

Yanfeng Shen and Carlos E. S. Cesnik[*]

Department of Aerospace Engineering, University of Michigan, Ann Arbor, MI, 48109, USA

ABSTRACT

This paper presents a parallelized modeling technique for the efficient simulation of nonlinear ultrasonics introduced by the wave interaction with fatigue cracks. The elastodynamic wave equations with contact effects are formulated using an explicit Local Interaction Simulation Approach (LISA). The LISA formulation is extended to capture the contact-impact phenomena during the wave damage interaction based on the penalty method. A Coulomb friction model is integrated into the computation procedure to capture the stick-slip contact shear motion. The LISA procedure is coded using the Compute Unified Device Architecture (CUDA), which enables the highly parallelized supercomputing on powerful graphic cards. Both the explicit contact formulation and the parallel feature facilitates LISA's superb computational efficiency over the conventional finite element method (FEM). The theoretical formulations based on the penalty method is introduced and a guideline for the proper choice of the contact stiffness is given. The convergence behavior of the solution under various contact stiffness values is examined. A numerical benchmark problem is used to investigate the new LISA formulation and results are compared with a conventional contact finite element solution. Various nonlinear ultrasonic phenomena are successfully captured using this contact LISA formulation, including the generation of nonlinear higher harmonic responses. Nonlinear mode conversion of guided waves at fatigue cracks is also studied.

Keywords: structural health monitoring, guided waves, nonlinear ultrasonics, contact model, LISA, fatigue crack, breathing crack, parallel computing

1. INTRODUCTION

Fatigue cracks exist as great menace to engineering structures and are considered as the precursors to catastrophic failures. Effective detection of fatigue cracks at their early stages, is thus of critical importance and particular interest [1]. However, unlike gross damage, the fatigue cracks are barely visible in its closed state, imposing considerable difficulty for the conventional ultrasonic techniques which are only sensitive to open cracks [2]. On the other hand, nonlinear ultrasonic techniques have shown much higher sensitivity to incipient structural changes with distinctive nonlinear features, such as higher/sub harmonic generation, DC response, mixed frequency modulation response (sideband effects), and various frequency/amplitude dependent threshold behaviors [3, 4]. The integration of nonlinear ultrasonic techniques into guided wave based interrogation procedures is drawing increasing attention from the Structural Health Monitoring (SHM) and Nondestructive Evaluation (NDE) communities, because such a practice inherits both the sensitivity from nonlinear NDE techniques and the large-area inspection capability from SHM guided waves [5].

To date, the research on nonlinear ultrasonics are generally experimental and more on non-dispersive bulk waves. Theoretical and numerical studies of the interaction between multi-modal dispersive guided waves and localized nonlinear structural damage are still limited. In order to achieve the optimum design of nonlinear guided wave based SHM system and the effective interpretation of the sensing signals, efficient computational models are needed. However, the simulation of nonlinear dynamics of the fatigue cracks itself is a challenging task; the multi-modal, dispersive, and complex mode conversion characteristics of guided waves further add to the difficulty.

To efficiently predict the nonlinear guided wave sensing signals, an analytical model based on the exact Rayleigh-Lamb solutions has been developed, simulating multi-modal Lamb waves interacting with a breathing crack [6]. But it is only a 1-D representation of the interaction phenomena and requires the input of multiple nonlinear interaction coefficients from other computational modules. To fully capture the 3-D nonlinear dynamics, finite element method (FEM) for contact-impact problems has been widely investigated, maturing over the years [7]. But the handling of massively large matrices inevitably result in heavy cost of computer resource and computational time even for explicit solving schemes. Moreover, the proper choice of contact parameters to achieve solution convergence and accuracy is always found to be challenging

---

[*] cesnik@umich.edu, Phone: (734) 764-3397, Fax: (734) 764-0798

and tedious, which requires extensive modeling experience. Time domain Boundary Element Method (BEM) has been explored as an efficient approach to solving Contact Acoustic Nonlinearity (CAN) by considering it as a boundary-type nonlinear problem, in which the nonlinear effect is contained in the boundary conditions only [8]. Current literature on BEM mainly addresses the interaction between contact cracks and bulk waves, yet modeling efforts on guided waves are still limited. Finite Difference (FD) method has also been reported for contact-impact analysis of crack surfaces with much less computational burden compared to conventional FEM [9]. The formulations presented in these studies mainly address the wave crack interaction in homogeneous materials. To solve wave propagation in heterogeneous materials, the Local Interaction Simulation Approach (LISA), based on FD formulation and Sharp Interface Model (SIM), has been developed. 1-D, 2-D, and 3-D LISA formulations were first developed for isotropic heterogeneous materials executed on Connection Machines [10, 11, 12]. LISA underwent considerable progress during the past decade, with its extension to general anisotropic materials [13, 14], coupled field capabilities [15], hybridization with other numerical methods [16, 17], and execution on powerful Graphics Processing Units (GPU) with Compute Unified Device Architecture (CUDA) technology [18].

Pioneer research on including nonlinear effects into LISA formulation has been conducted using a spring model in 1-D, 2-D, and 3-D cases [19, 20, 21]. This spring model LISA formulation altered the material at the crack location between continuous and discontinuous to simulate the crack close and open phenomena during wave crack interaction. It successfully captured the local nonlinearity, but it did not consider the possible stick-slip contact scenario. The fact that rough contact surfaces have distributed microscopic initial openings and closures was also not considered. Alternative approach other than the spring model is desired to improve current nonlinear LISA solutions.

In this study, we developed a 3-D LISA scheme to simulate the nonlinear interactions between guided waves and fatigue cracks. A Coulomb friction model is integrated to capture the stick-slip contact scenario. The numerical scheme is implemented using CUDA and executed on GPU, achieving high computational efficiency. After the introduction of the theoretical formulation, the implementation of the 3-D contact LISA is discussed, followed by convergence study and numerical verifications. The numerical case studies address several interesting aspects in wave crack interaction: (1) generation of higher harmonics and DC response; (2) nonlinear mode conversion at fatigue cracks.

2. THEORETICAL FORMULATION AND SOLUTION APPROACH

This section illustrates the theoretical fundamentals and formulation of the proposed LISA modeling technique to simulate the nonlinear interactions between guided waves and fatigue cracks. The penalty method for contact problems is discussed first. Then, the integration of contact dynamics into LISA framework is presented.

2.1 Penalty method for contact problems

Penalty method is initially investigated to solve constrained optimization problems and have been adopted as one of the primary approaches to simulate contact problems in FEM. It approximates a constrained problem by an unconstrained one whose solution ideally converges to the solution of the original constrained problem. This convergence is achieved by punishing the violation of these constrains.

Figure 1 illustrates the principle of using penalty method to approximate contact continuum mechanics. From a strict dynamics perspective, the kinematic axiom enforces the impenetrability condition. When the two bodies are in contact with each other, the material points on their boundaries may coalesce during the motion of the bodies. If they are not in contact, they will be treated as separate systems. When the two bodies are in contact, they will interact with each other through the contact compressional tractions, i.e., no tensile tractions can occur.

Utilizing the penalty method, the impenetrability condition is weakened; a small amount of penetration is allowed to enable the mathematical formulation. This penetration can be easily identified as the measurement of violation against the impenetrability condition and is penalized by introducing a contact stiffness that tends to minimize this violation. When an appropriate contact stiffness is reached, the amount of the penetration approaches zero, which makes the numerical solution converges towards the physical contact phenomena.
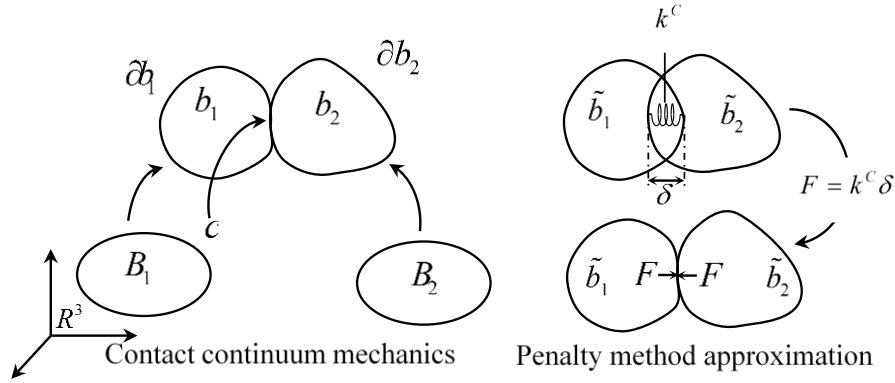
Figure 1: Using penalty method to approximate contact dynamics.

2.2 Adding contact dynamics into LISA

LISA is a finite-difference based numerical simulation method. It approximates the partial differential elastodynamic equations with finite difference quotients in the discretized temporal and spatial domains. The coefficients in LISA iterative equations (IEs) depend only on the local physical material properties. The Sharp Interface Model (SIM) enforces the stress and displacement continuity between the neighboring computational cells and nodes. Therefore, changes of material properties in the cells surrounding a computational node can be captured through these coefficients. A typical computational node and its surrounding cells/nodes are shown in Figure 2. The final IEs determine the displacements of a certain node at current time step based on the displacements of its eighteen neighboring nodes at previous two/three time steps, depending on whether material damping is considered. For details of the derivation for the LISA IEs, the readers are referred to Ref. [14].
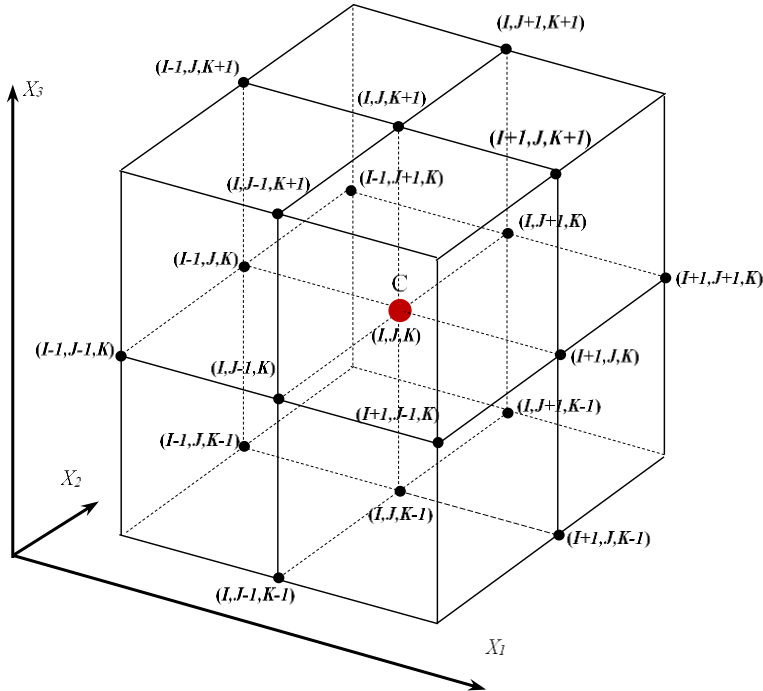

Figure 2: A generic node C at location (I, J, K) with eighteen nearest neighboring nodes (adopted after Ref. [14]).

A typical contact procedure during wave crack interaction can be categorized into four consecutive stages: (1) pre-contact state, where the contact surfaces are separate from each other and are subjected to free boundary conditions; (2) contact initiation, where contact counterparts meet, which triggers the exertion of contact forces; (3) in-contact motion, where the crack surface moves together in a stick-slip pattern, with interactive contact forces; (4) contact pair separation, where the

contact counterparts leave each other, releasing the contact interactions and regaining the free boundary conditions. It can be noticed that the boundary condition of the contact surfaces alters between free and constrained situations.

To satisfy the alternating boundary conditions at the contact surfaces, special design and treatment on the computational grid is needed. In conventional LISA technique and the previous nonlinear spring model, the structural discretization is continuous [19, 20]. In this study, a discontinuous mesh to model the crack surfaces is used. The structural discretization was carried out using the commercial FEM software ANSYS 14. Then, a model converter was programed using CUDA C to convert the nodal connectivity and material allocation from the format of FEM to that of LISA. During such a conversion procedure, three additional efforts were made to prepare the LISA computational grid for the contact analysis, including contact pair recognition, normal direction detection, and auxiliary air cell addition. Figure 3a shows the discontinuous mesh with separate nodes along the contact surface. A pair of nodes located on the counterpart of the crack surface is designated as a contact pair. The contact forces will be acted interactively on the contact pair nodes. Figure 3b shows a generic contact node and its normal direction with respect to the contact surface. It should be noted that since LISA uses a structured mesh, there will be six normal directions appearing in each contact pair, i.e., *+x, -x, +y, -y, +z, -z*. In practice, curved surfaces can be approximated by fitting the structured mesh to the target geometry using dense discretization [22]. Figure 3c illustrates the addition of auxiliary air cells to the LISA computational grid surrounding the contact nodes to satisfy a free boundary condition when the contact surfaces are separate from each other and immersed in air. It can be seen that five auxiliary nodes and four air cells are added to each contact node. Comparing Figure 3c with Figure 2, one can realize that by adding the auxiliary cells, a special contact surface node is brought to the unified LISA computation representation with eighteen neighboring nodes. It should be noted that the air cells on the contact surfaces are not implemented during structural discretization in ANSYS but are generated during the model conversion procedure. When the crack surfaces come into contact, penalty contact forces are acted on the contact nodes to constrain the in-contact motion. In this way, the modeling of the alternating boundary condition can be achieved.

Contact pair recognition Normal direction detection Adding auxiliary air cells
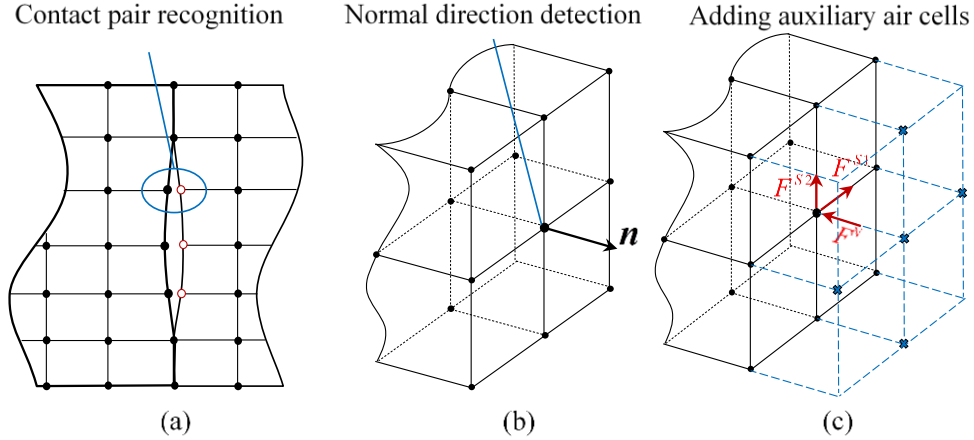

(a)   (b)   (c)

Figure 3: Special treatment on the computational grid: (a) using discontinuous mesh to model contact surfaces; (b) detecting the normal direction at a generic contact node; (c) adding auxiliary air cells and contact forces to satisfy the alternating boundary conditions.

To incorporate contact forces into the LISA formulation, consider the elastodynamic equations:

$$\partial_l \left(S_{klmn} w_{m,n} \right) + f_k = \rho \ddot{w}_k, \quad k,l,m,n = 1,2,3 \tag{1}$$

where S_{klmn} is the stiffness tensor, w is the displacement field, f is the body force, and ρ denotes the material density. From the layout of Figure 3c, the contact forces can be converted into equivalent body force terms in Eq. (1). Following the standard LISA derivation procedure, Eq. (1) can be transformed using customary FD transformations for second-order space and time derivatives. Sharp Interface Model is used to enforce the displacement and stress continuity at interfaces of material inhomogeneity. Linear combination of the equations leads to the final LISA iterative equations for three displacement components. Detailed LISA IE derivation procedure has been reported in the literature (e.g., Ref [14]) and thus is omitted here. The final IEs of displacements with body force terms can be expressed in a general form as

$$W_k^{t+1} = \psi \left(W_i^t, W_j^t, W_k^t, W_k^{t-1} \right) + W_k^f \tag{2}$$

where the resulting displacement W_k^{t+1}, in k direction at the target time step $t+1$, depends on itself and its neighboring nodes at the previous two time steps. For detailed derivation and explicit form ψ, the readers are referred to Ref [14]. For the purpose of this study, the focus is on the body force induced displacement term W_k^f at the contact node (I, J, K), which is given by

$$W_k^f = \frac{\chi}{8} \sum_{\alpha, \beta, \gamma = \pm 1} f_k^{I+\alpha, J+\beta, K+\gamma} = \chi \cdot \bar{f}_k^{I,J,K} \tag{3}$$

where $\chi = \Delta t^2 / \bar{\rho}$, with Δt being the time step and $\bar{\rho}$ being the average density of all the eight cells surrounding node (I, J, K) and $\bar{f}_k^{I,J,K}$ denotes the average body force over the volume enclosed by the eight neighboring cells.
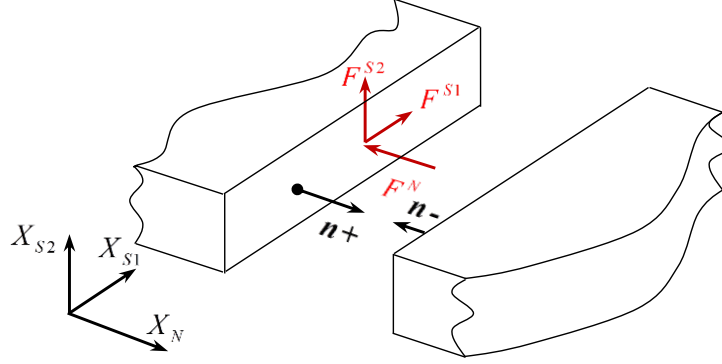

Figure 4: General local contact coordinate with respect to the contact surface orientation.

Figure 4 shows the general local contact coordinate with respect to the contact surface orientation for the derivation of contact forces. The penalty method states that in order to punish the relative penetration δ, the contact force can be casted into the form of $F = k^C \delta$, where k^C is the contact stiffness. When solving for the shear contact force in stick motion, δ can be generalized to relative shear violation. Between two contact surfaces, three contact forces may exist: a normal direction component and two shear direction components. In a local contact coordinate system, the normal contact force can be written as

$$F^N = \Theta(\delta^N) \Lambda^N k_N^C \frac{\delta^N}{\Delta x_N} \Delta x_{S1} \Delta x_{S2} \tag{4}$$

where $\Theta(\delta^N)$ is a control parameter taking the value of either one or zero, corresponding to in-contact and separate situations, respectively; Λ^N is the normal contact stiffness multiplier; k_N^C is the normal contact stiffness/modulus; δ^N is the contact condition violation (normal penetration in this case); $\Delta x_N, \Delta x_{S1}, \Delta x_{S2}$ are the spatial cell sizes along three local contact coordinate axes. The term $\delta^N / \Delta x_N$ can be interpreted as the normal contact strain. The term $\Delta x_{S1} \Delta x_{S2}$ represents the effective area on which the contact stress acts. Thus, the meaning of Eq. (4) is straight forward.

The shear contact force F^{S1} in X_{S1} direction is given by

$$F^{S1} = \Theta(\delta^N) \Lambda^S k_{S1}^C \frac{\delta^{S1}}{\Delta x_N} \Delta x_{S1} \Delta x_{S2} \tag{5}$$

where Λ^S is the shear contact stiffness multiplier; k_{S1}^C is the shear contact stiffness/modulus; δ^{S1} is the shear violation in X_{S1} direction; The term $\delta^{S1} / \Delta x_N$ can be interpreted as the engineering shear contact strain. And similarly,

$$F^{S2} = \Theta(\delta^N) \Lambda^S k_{S2}^C \frac{\delta^{S2}}{\Delta x_N} \Delta x_{S1} \Delta x_{S2} \tag{6}$$

After obtaining the contact forces at the contact nodes, the contact forces can be converted into the equivalent body forces. According to the definition of body force, we need to evaluate the contact force per unit volume, i.e.,

$$\bar{f}_k = F_k \big/ \left(\Delta x_N \Delta x_{S1} \Delta x_{S2} \right)$$

(7)

where $\Delta x_N \Delta x_{S1} \Delta x_{S2}$ is the nominal volume that encloses each contact node. In this way, the contact LISA formulation can be obtained.

A Coulomb stick-slip contact motion is considered in this study. Figure 5 shows the Coulomb friction model. μ_S and μ_D denote the static and dynamic friction coefficients. The critical condition between stick and slip contact motions can be expressed as

$$\sqrt{\left(F^{S1} \right)^2 + \left(F^{S2} \right)^2} > \mu_S F^N$$

(8)

When this condition is satisfied, the slip contact motion is triggered. In such a case, the normal contact force will not be influenced and still take the same form as before. However, the shear contact forces will be the sub-components of the dynamic friction force developed between the contact surfaces. It should be noted that, compared with the stick contact motion, the estimation of shear violations δ^{S1} and δ^{S2} also changes and the shear violations need to be updated for every time step during the slip contact motion. The judging criterion in Eq. (8) also need to be tested for each time step.
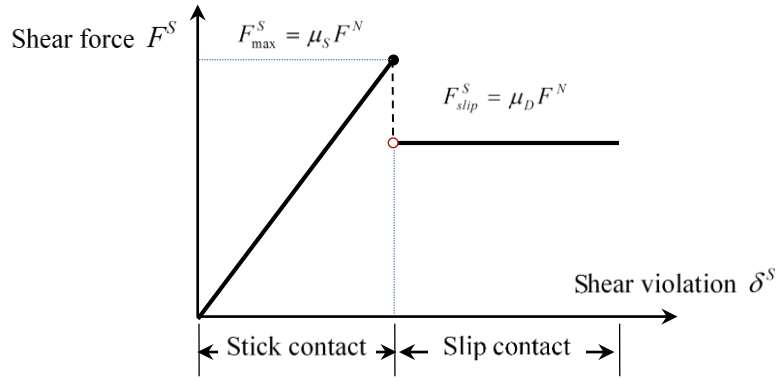

Figure 5: Stick-slip contact motion governed by Coulomb friction model.

3. NUMERICAL IMPLEMENTATION

Figure 6 shows the numerical algorithm flow chart for the formulation implementation. When the discretization grid enters the model converter, contact pairs are recognized and associated information collected such as contact pair node number, contact surface normal direction, auxiliary nodes and cells, etc. When the solving procedure starts, judgement on the penetration is performed. If the contact nodes are separate from each other, then no contact force acts on the counterparts of the contact pair. On the other hand, if penetration is detected in a contact pair, then contact forces need to be exerted on the contact nodes. A secondary judgement on the stick-slip motion is performed based on Eq. (8). If the stick motion takes place, then the shear force needs to be estimated through the shear violation based on the initial stick position. However, if the slip motion takes place, then the shear force needs to be evaluated through the shear violation based on the previous step. During the stick-slip contact motion, the shear violation must be updated for each time step and the motion criterion needs to be evaluated according for each time step.

In this study, the contact LISA algorithm was implemented using CUDA technology and executed the computation in parallel in GPUs (NVIDIA GeForce Titan of 2688 CUDA cores with 28672 concurrent threads). There are two major characteristics of the current contact LISA formulation that enables the computation to be expedited. First, LISA is massively parallel. This is because the computation of a general node or a contact node only depends on the solutions of its eighteen neighboring nodes at the previous two time steps. Thus, the behavior of each node is independent from the others at the target time step, i.e., the computation of each node can be carried out individually in parallel. Second, the wave propagation simulation tasks usually require dense discretization of the structure, resulting in a computationally intensive problem. GPUs, with their massive concurrent thread feature, are suitable to handle such large size problems by

distributing the workloads among a large number of functional units and carry out highly efficient parallel computing. During the computation, the parameters are first established in the host memory (RAM). Then a copy of these parameters is sent to the device memory (GPU global memory) for it to be processed. The computation of each node is assigned to a functional thread, i.e., each thread gathers the displacements of its eighteen neighboring nodes and one contact pair node (if identified as a contact node) at previous two time steps, process the material properties in the eight surrounding cells, and execute the kernel to compute the displacements of this node at the target time step. Since one of the bottlenecks of a CUDA program is the data transfer between the device memory and host memory, results are transferred from the GPU to the CPU only sporadically (every 20-30 steps depending on the frequency of the propagating waves) to minimize such data transfer.
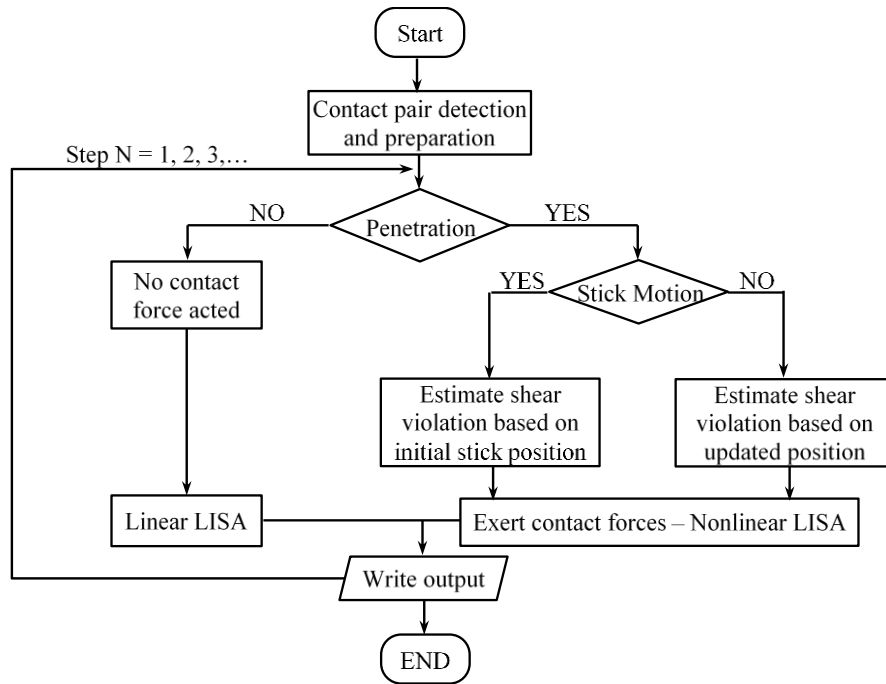

Figure 6: Contact modeling implementation process.

4.   CONVERGENCE STUDY AND NUMERICAL VERIFICATION

In this section, a convergence study on the contact LISA formulation is presented. Guidelines for the proper choice of computational parameters for an accurate and converged solution are given. Theoretical values of contact stiffness are derived first as the initial guess to feed into the model. The proper range of contact stiffness multipliers is tested by observing the convergence behavior of contact solutions. Then, a benchmark problem is simulated by the contact LISA model and verified against the solution from ANSYS.

4.1 Proper choice of contact parameters

The values of contact stiffness have been found to directly influence both the convergence and the accuracy of the results in penalty method based contact models [7]. In general, a low contact stiffness will produce an inaccurate solution with large contact surface penetration, violating the impenetrability condition. With the increment of contact stiffness, the violation will become smaller and smaller, which makes the solution converge towards the physical contact condition and arrive at an accurate region. However, when the contact stiffness exceeds a certain value, different adverse solution behaviors may be observed in FEM and contact LISA. For the case of FEM simulations, excessive contact stiffness may result in the ill-conditioning of the stiffness matrix, which usually causes solution convergence difficulty. For the contact LISA formulation, the contact surfaces may violently jump away from each other upon contact, deviating its physics and accurate solution. Thus, it is critical to choose proper values of contact stiffness in order to obtain accurate contact solutions. The proposed process starts with a theoretical contact stiffness using a simplified model as the initial point and adjust the stiffness multipliers to find the range of parameters for accurate solutions.
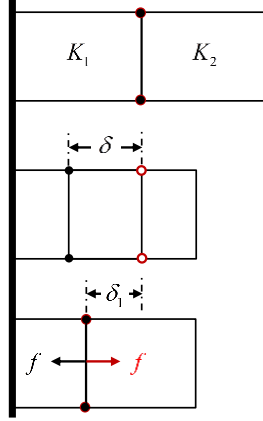
Figure 7: Simplified model of ideal contact force eliminating penetration.

Figure 7 shows two elastic bodies with general stiffness values of K_1 and K_2, respectively. The body on the left hand side is a fixed target, while the right hand side is a contactor. Due to body motion, a penetration δ is introduced when no contact force is applied. Then two contact forces f with the same magnitude but opposite directions are applied on the contact surfaces. The contact forces with the ideal value will eliminate the penetration between the two bodies. The equilibrium equations satisfying this condition can be written as

$$\begin{cases} K_1\delta_1 = f \\ K_2\left(\delta - \delta_1\right) = f \end{cases} \tag{9}$$

Cancelling the term δ_1 in Eq. (9) yields

$$\frac{K_1 K_2}{K_1 + K_2}\delta = f \tag{10}$$

By identification, the initial value of contact stiffness in LISA can be estimated to be

$$k_{ii}^C = \frac{\left(\dfrac{1}{4}\sum_{\alpha,\beta,\gamma=\pm 1}\tilde{S}_{ii}^{CONTA}\right)\left(\dfrac{1}{4}\sum_{\alpha,\beta,\gamma=\pm 1}\tilde{S}_{ii}^{TARGE}\right)}{\dfrac{1}{4}\sum_{\alpha,\beta,\gamma=\pm 1}\tilde{S}_{ii}^{CONTA}+\dfrac{1}{4}\sum_{\alpha,\beta,\gamma=\pm 1}\tilde{S}_{ii}^{TARGE}} \qquad i = 1, 2, 3, 4, 5, 6 \tag{11}$$

where $\tilde{S}_{ii}^{CONTA}$ and $\tilde{S}_{ii}^{TARGE}$ represent the diagonal terms of the stiffness matrix of the contactor and target materials. $\tilde{S}_{ii} = S_{ii}\left(i+\alpha, j+\beta, k+\gamma\right)$ denotes the stiffness component in one of the eight cells surrounding the point (i, j, k) depending on the choice of (α, β, γ) from $(+1, -1)$. Since for each contact node, four of its neighboring cells are auxiliary air cells with negligible stiffness contribution, thus the average effective stiffness need to be computed using the four solid material cells. And this is the reason why the factor of one quarter is chosen.

After the initial estimation of contact stiffness at each contact pair contact stiffness multipliers Λ^N and Λ^S are assigned to the corresponding stiffness values. By adjusting these parameters, the range can be found where solutions converge with coherent contact behavior.

Figure 8 shows the model setup of solution convergence test. It consists of a 500-mm long, 20-mm wide, and 5-mm thick aluminum strip. A 10-mm long through-thickness breathing crack is located in the center of the strip. A pair of in-phase line prescribed displacements (1 µm peak to peak value) is used to generate 100-kHz 10-cycle tone burst S0 guided waves into the structure. They will propagate along the structure, interact with the breathing crack, bring the crack information with them, and are finally picked up at the sensing point. The out-of-plane displacement at 10 mm right after the crack was recorded and post-processed for the convergence study.
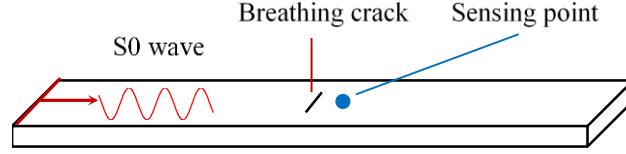
Figure 8: Schematic of model setup of solution convergence test for the proper choice of contact stiffness.

The contact stiffness multipliers Λ^N and Λ^S were simultaneously increased from 0 to 7 with a step of 0.2. The consecutive two solutions at the sensing point before and after an increment were compared. The difference between these two solutions were measured by the L2-norm based relative ratio

$$R^{L2} = \sqrt{\frac{\sum_{j=1}^{N}\left[s_i(j) - s_{i-1}(j)\right]^2}{\sum_{j=1}^{N}s_{i-1}^2(j)}} \qquad (12)$$

where s_i and s_{i-1} represents the signal before and after the ith increment of the multipliers. N is the time data length.

Figure 9 shows the convergence study results as well as the contact behavior under various ranges of stiffness multiplier. The solution is assumed to have converged when the R^{L2} drops below 5%. Thus, the suggested range of the contact stiffness multiplier is between 0.8 and 3.4. It can be noticed that the theoretical initial estimation of the contact stiffness worked well in terms of solution convergence. In terms of contact behavior, when the contact stiffness is low, large penetration will happen between the contact surfaces, violating the impenetrability condition and resulting in inaccurate solutions. With an appropriate contact stiffness, the contact surfaces interact with each other coherently. When the contact stiffness becomes excessively large, contact surfaces may violently jump away from each other upon interaction, which is not physically plausible. This jumping phenomena happens because the selected time step is not small enough to fully capture the interaction and stabilize the contact pair penetration behavior.
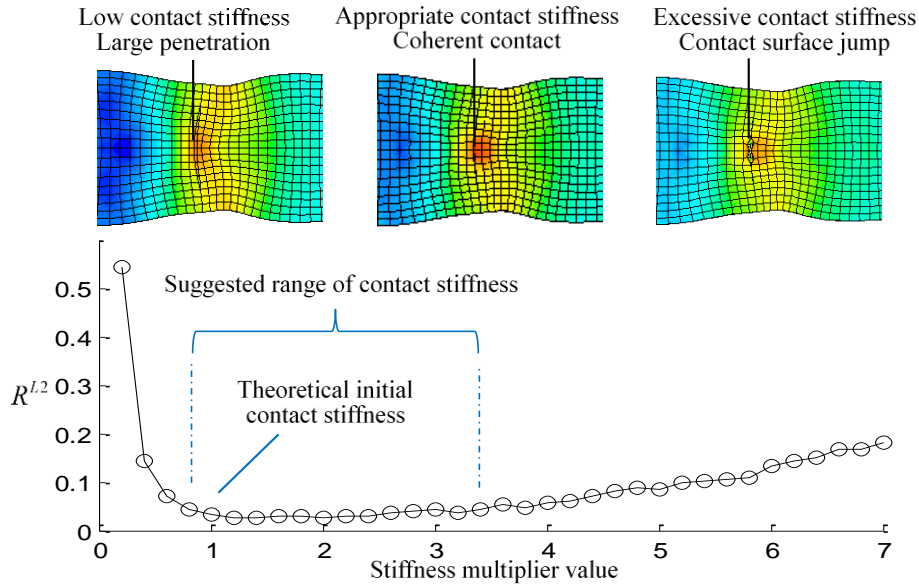

Figure 9: Convergence and contact behavior study: low contact stiffness results in large penetration; appropriate contact stiffness render coherent contact; excessive contact stiffness causes contact surface jump.

Figure 10 presents the comparison between the results using $\Lambda = 0.8$ and $\Lambda = 3.4$. It should be noted these two contact stiffness multipliers bounded the lower and upper limits of the suggested contact stiffness range for solution convergence and coherent contact behavior. The results agree well with each other in both the time domain signal and the frequency domain spectrum. Heavy distortions in the time domain signals can be observed due to the nonlinear interaction between guided waves and the breathing crack. In the frequency domain spectra, one can notice the fundamental excitation

frequency component at f_c as well as the nonlinear higher harmonics $2f_c, 3f_c$, and so on. The DC response at low frequency range can also be clearly identified. The differences in the spectra only appeared at much higher frequencies.
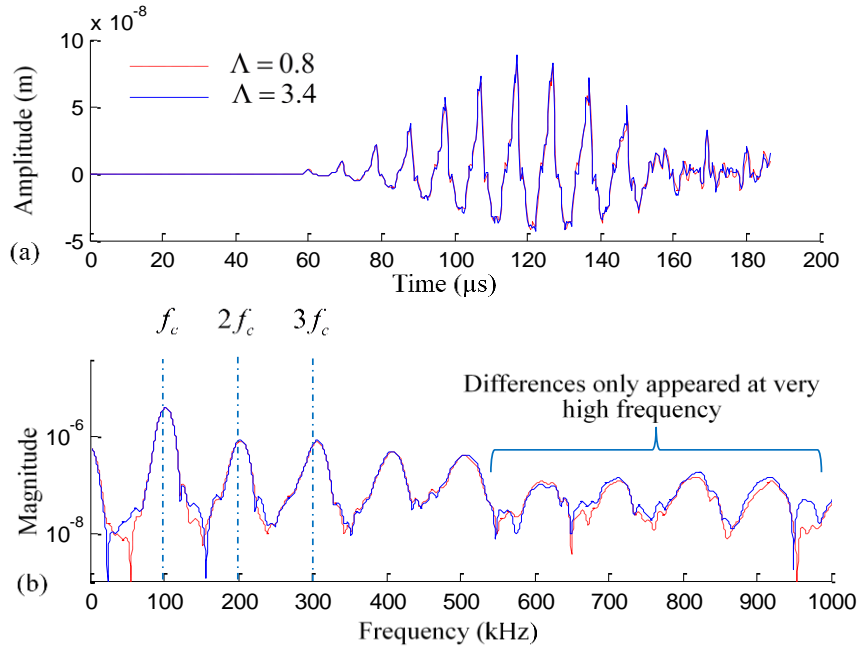

Figure 10: Solutions within the converged contact stiffness range agree well with each other ($\Lambda = 0.8$ and $\Lambda = 3.4$): (a) time domain simulation signals; (b) frequency domain spectra.

4.2 Numerical verification against finite element solution

To verify the contact LISA model, a benchmark simulation for the setup described in Figure 8 is conducted and the solution compared with the result from ANSYS 14. The ANSYS contact model used SOLID45 eight node structural element to discretize the geometry and CONTA173/TARGE170 contact elements to model the crack surfaces. Element size of 1-mm for the in-plane and across the thickness directions was used. The mesh size l_e was checked against the shortest wavelength $\lambda_{\min}$ possible at the third harmonics, i.e., $l_e \leq \lambda_{\min}/20$. A time step Δt of 0.125 µs was utilized for the time marching Newmark-beta integration to ensure the accuracy up to the third harmonic frequency, i.e., $\Delta t \leq 1/20 f_{\max}$. In the LISA model, the cell size was 1 mm in the in-plane direction and 0.5 mm across the thickness. The time marching step was 0.06 µs obtained from the CFL number requirement [14]. The stiffness multiplier values were set to 1.4.

Figure 11 shows the verification of the contact LISA model against the ANSYS solution. It can be noticed that the signals agree with each other in time domain with merely slight differences. The frequency spectra shown in Figure 11b also demonstrated that the frequency components of fundamental excitation, low frequency DC component, second, third, even fourth higher harmonics compare very well with each other. Differences only appeared at very high frequency range, where the time step is sufficiently small to generate accurate results or meaningful comparison between the two methods. This numerical verification against commercial finite element code attested the capability and validity of the new contact LISA model.

It should be noted that the new contact LISA model also achieved much higher computational efficiency over the conventional nonlinear FEM simulation. Both computational tasks were conducted on an Asus ESC2000 G2 workstation with a 2.00 GHz Intel Xeon E2-2650 processor, 32 GB of 1.60 GHz memory, and an Nvidia GeForce GTX Titan graphics processor with 2688 CUDA cores. The FEM simulation with 279,900 degrees of freedom took around 19 seconds for each time step, resulting in a total computational time of 8 hours for 1500 time steps. On the other hand, LISA simulation with 648,120 degrees of freedom merely consumes around 0.043 second for each time step, resulting in a total computational time of 2.15 minutes for 3000 time steps. Thus, it is apparent that the new contact LISA model is much more efficient than the conventional nonlinear FEM simulation, while achieving comparable results.
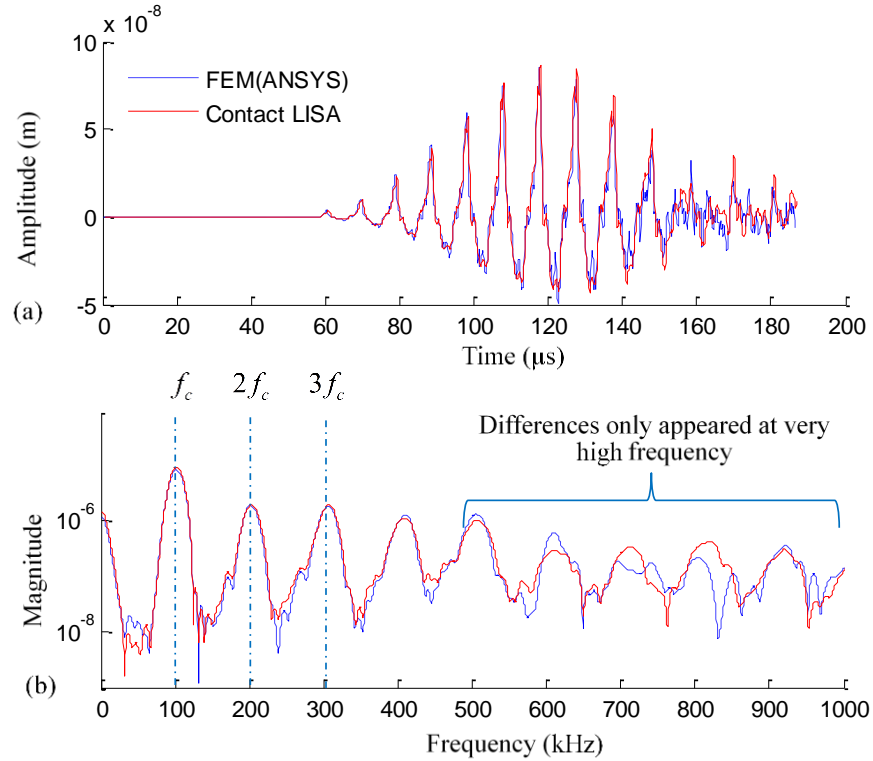
Figure 11: Contact LISA solution compares well with the result from commercial FEM package ANSYS: (a) time domain simulation signals; (b) frequency domain spectra.

5. NUMERCIAL STUDY OF GUIDED WAVE INTERACTION WITH FATIGUE CRACKS

After laying out the theory behind the new contact LISA model, numerical case studies are conducted on the nonlinear phenomena introduced by the interaction between guided waves and fatigue cracks.

5.1 Nonlinear higher harmonics and DC response: linear vs. nonlinear interactions

This numerical case study aims to demonstrate the classical nonlinear higher harmonic and DC component generation phenomena during the nonlinear interaction between guided waves and a fatigue crack. This situation is compared with the linear interaction between guided waves and a notch, where the notch surfaces will not come into contact. Again, the model setup described in Figure 8 is adopted. The only difference is that it contains additional air cells to model the notch. A 10-cycle 100-kHz tone burst excitation is used to generate pure S0 Lamb mode into the structure. Figure 12 shows the time trace of the excitation signal and its frequency spectrum.
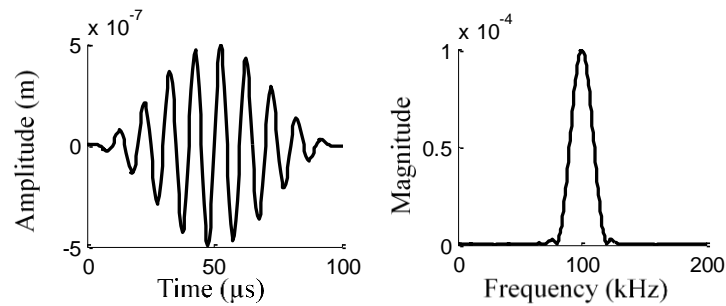

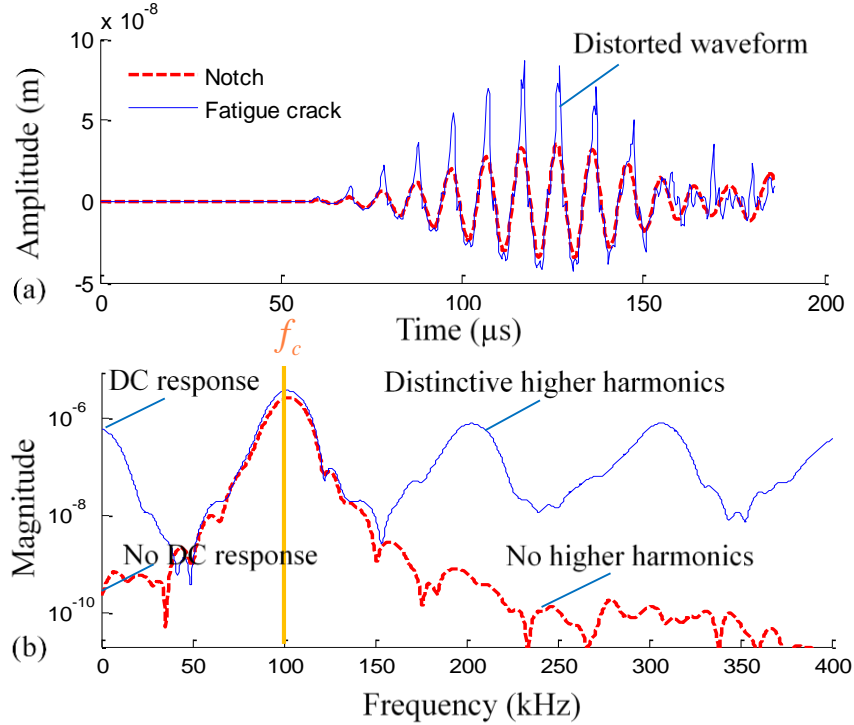Figure 12: Excitation signal: (a) time domain; (b) frequency domain spectrum.

Figure 13: The interaction of guided waves with a fatigue crack brings in distinctive nonlinear higher harmonics, while their interaction with a notch does not. (a) Time trace comparison; (b) frequency spectrum comparison.

Figure 13 presents the simulation results, comparing the sensing signals between the notch crack and the fatigue crack cases. It can be noticed that the time trace of the notch crack case resembles the waveform of the excitation signal with balanced positive and negative oscillatory amplitudes. In contrast, the time trace from the fatigue crack case is heavily distorted with impact induced high amplitude sharp peaks and a low frequency modulation. The waveform also shows zigzags, unlike the smooth pattern present in the notch crack case. The frequency spectra of these two signals show great difference too. It can be observed that the notch crack signal spectrum shows only the excitation frequency component at 100 kHz. No higher harmonics nor DC component exist. On the other hand, the fatigue crack signal presents distinctive nonlinear higher harmonics and DC component in its spectrum. The generation of higher harmonics and DC component is a classical nonlinear phenomenon and it serves as the basis for many nonlinear ultrasonic inspection methodologies. The new contact LISA model is capable of simulating such nonlinear ultrasonic signals.

5.2 Nonlinear mode conversion at fatigue cracks

When guided waves interact with structural damage, mode conversion may happen, transforming one wave mode into another. The nonlinear contact-impact dynamics during wave interaction with fatigue cracks will give rise to even more complicated mode conversion phenomena. Figure 14 shows the model setup utilized to study such mode conversion effects at fatigue cracks. It consists of a 400-mm long, 200-mm wide, and 5-mm thick aluminum plate. The excitation points located on the top and bottom surfaces near the boundary to selectively generate symmetric and antisymmetric Lamb modes and minimize reflections. A 10-mm long fatigue crack resides in the center of the plate. Frequency-wavenumber analysis is deployed to analyze the wave mode components propagating through the crack. In Figure 14, the analysis of path A provides the information on the mode type incident to the fatigue crack before its interaction with the damage, while path B is used to analyze the converted wave modes after the interaction.

Figure 15 shows the time and frequency domain representation of the excitation signal used in this study, as well as the frequency wavenumber dispersion curves of Lamb waves in the 5-mm thick aluminum plate. A 250-kHz 5-cycle tone burst excitation is used that mainly generates the fundamental symmetric mode (S0) and antisymmetric mode (A0) into the structure. The complexity of mode conversion at fatigue cracks arises from the generation of higher harmonics, which spans the high frequency range containing higher wave modes. Thus, mode conversion will not only happen between S0 and A0 wave modes at the fundamental excitation frequency as the case of linear interaction, but also among A1, S1, S2,

A2, and etc. at the higher harmonic components as well. In this particular example, mode conversion into A1 at $2f_c$ may be possible since the second harmonic frequency is beyond A1's cut-off frequency. At $3f_c$, mode conversion into A2, S1, and S2 become possible. The mode conversion will involve even more modes with a greater number of higher harmonic components considered. It should be noted that the mode conversion not only depends on possible wave modes that may exist at corresponding higher harmonic components, but also determined by the incident wave mode and the fatigue crack geometric features. In this study, S0 or A0 waves are generated selectively into the structure and the mode conversion characteristics at a through-thickness crack are studied.
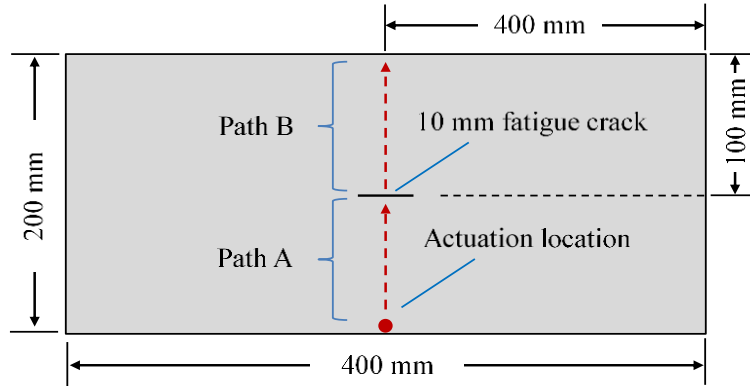

Figure 14: Model of 5-mm thick aluminum plate, showing two wave paths for wavenumber analysis: path A for analysis before the interaction; path B for analysis after the interaction.
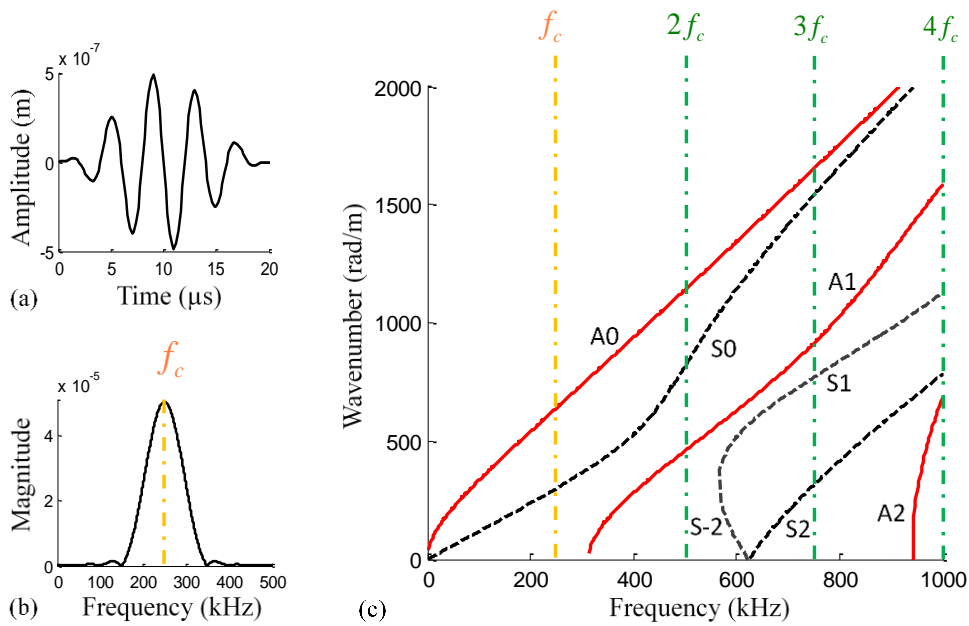

Figure 15: Nonlinear response may bring in higher modes: (a) time domain excitation signal; (b) frequency domain spectrum of the excitation; (c) wavenumber curves of the 5-mm thick aluminum plate showing possible wave modes at higher harmonic components.

Figure 16 presents the results for S0 wave interaction and mode conversion at a through-thickness fatigue crack. The wave propagation snapshots of out-of-plane displacement were captured, showing S0 wave generation, propagation, and scattering at the fatigue crack. It can be observed that the transmitted main wave front shows shadings due to the interference with the scattered wave field. It was found that the scattered wave field possesses several wave components with different wavelengths and group velocities, which may stem from the higher harmonic components of the same wave mode or the converted wave modes. The frequency-wavenumber analysis of the time-space domain wave field allows us to identify the wave modes participating in the propagation. Since we selectively excited the S0 mode, we can only find

the S0 wave component in the frequency-wavenumber analysis of path A. On the other hand, the frequency-wavenumber analysis of path B shows that higher harmonic components of S0 appeared at 500 kHz ($2f_c$) and 750 kHz ($3f_c$); S2 wave mode components were also found due to mode conversion at 750 kHz ($3f_c$) and 1000 kHz ($4f_c$), while no antisymmetric wave mode appeared from mode conversion. The rationale behind such phenomena is that the through-thickness crack and S0 wave motion are both symmetric with respect to the mid-plane of the plate, which will not introduce antisymmetric disturbances to generate antisymmetric wave modes. The existence of converted wave modes depends on the coupling of contact-impact traction distribution and the corresponding mode shapes. This also implies that the mode shape of S1 waves do not couple well with the contact-traction distribution during the wave damage interaction.
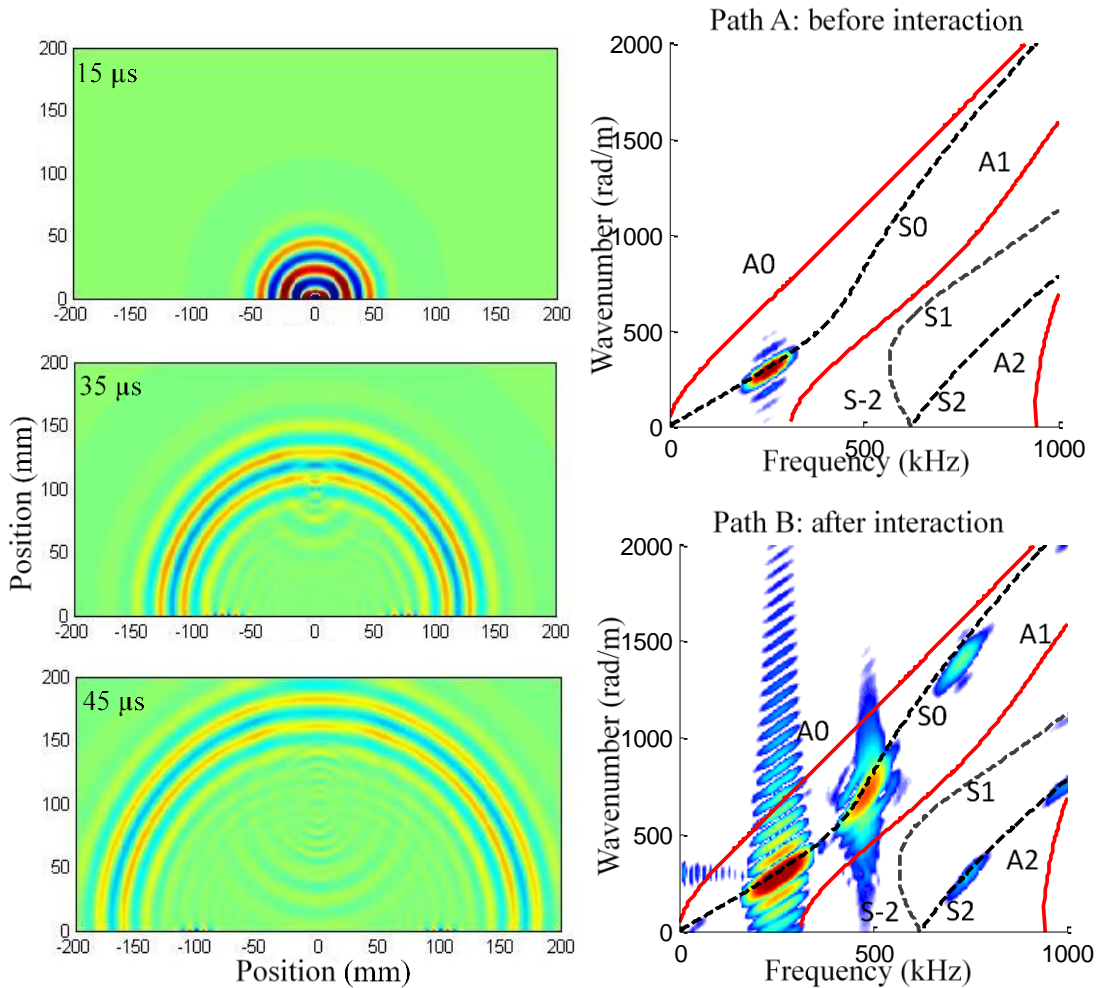

Figure 16: S0 wave interaction and mode conversion at a through-thickness fatigue crack.

Figure 17 presents the results for A0 wave interaction and mode conversion at a through-thickness fatigue crack. Guided wave generation, propagation, and scattering from the crack are shown in the snapshots from LISA simulation. The frequency-wavenumber analysis of path A shows that the main incident wave component is A0 mode. The frequency-wavenumber analysis of path B demonstrates that A0 mode did not appear at 500 kHz ($2f_c$). Instead, S0 waves from mode conversion showed up at 500 kHz. A0 and A1 mode appeared at 750 kHz ($3f_c$) and S0 mode was present at 1000 kHz ($4f_c$). The mode conversion phenomenon presents an alternating participation pattern between symmetric and antisymmetric modes at higher harmonic frequencies. It can be concluded that an antisymmetric incident wave mode will generate both antisymmetric and symmetric modes at a through-thickness fatigue crack. The rationale behind the alternating mode conversion is that, during one cycle of A0 wave interaction with the crack, the off-mid-plane contact-impact will happen twice, introducing two cycles of symmetric impact and one complete cycle of antisymmetric impact.
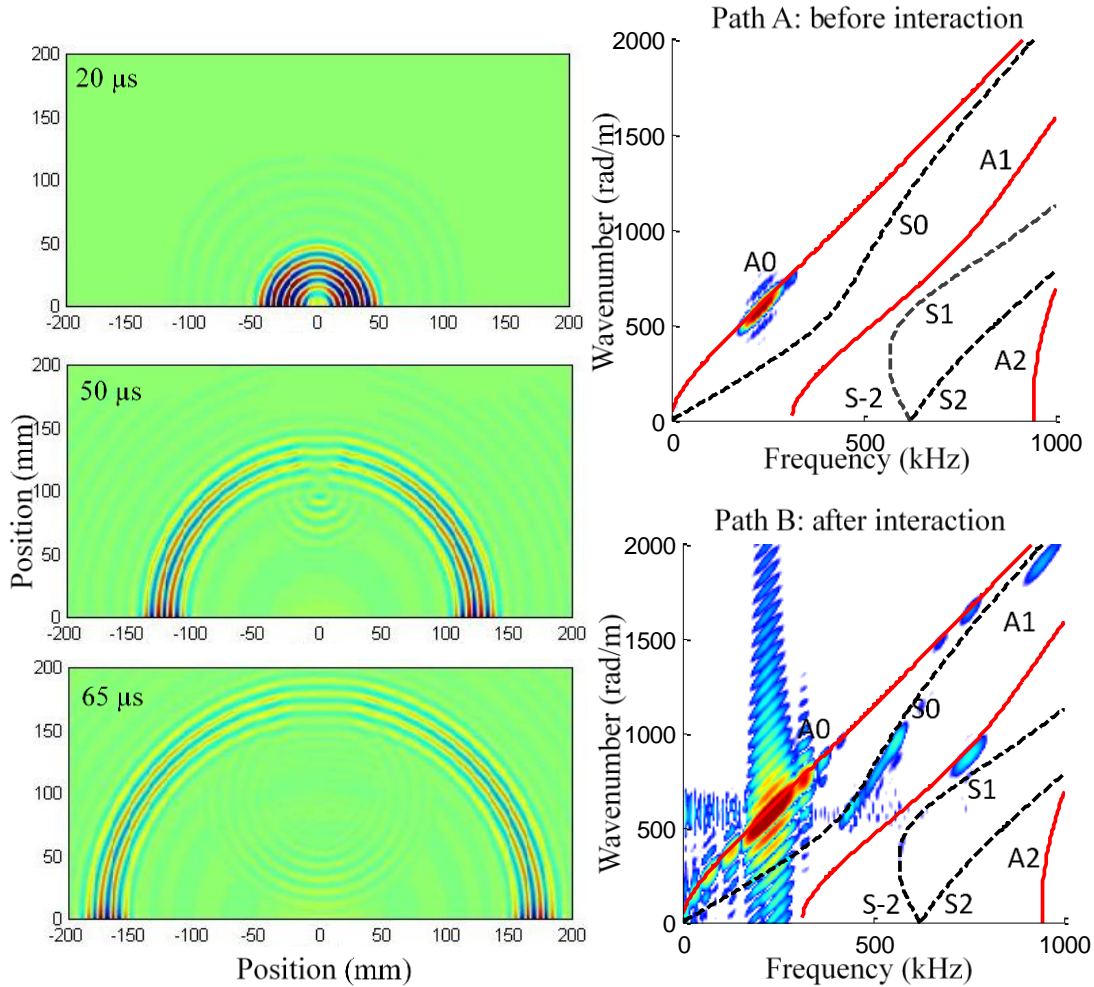
Figure 17: A0 wave interaction and mode conversion at a through-thickness fatigue crack.

6.   CONCLUDING REMARKS

In this study, a parallel algorithm to model the nonlinear dynamic interactions between ultrasonic guided waves and fatigue cracks was developed. This algorithm is based on the Local Interaction Simulation Approach (LISA) and penalty method. A Coulomb friction model was integrated to capture the stick-slip contact motions between the crack surfaces. The LISA procedure was parallelized via the Compute Unified Device Architecture (CUDA) and executed on powerful graphic cards. The explicit contact formulation, the parallel algorithm, as well as the GPU-based implementation facilitated LISA's superb computational efficiency over the conventional finite element method (FEM). Guidelines for the proper choice of contact parameters were given. The numerical verification against ANSYS showed good agreement between the new contact LISA model and finite element method. It also demonstrated that the new contact LISA model achieved much higher computational efficiency than the conventional FEM simulation.

Numerical case studies were conducted on Lamb wave interaction with fatigue cracks. Several nonlinear ultrasonic aspects were addressed. The classical nonlinear higher harmonic and DC responses were successfully captured. It was found that the generation of higher harmonic and DC component would only happen during the nonlinear interaction between guided waves and fatigue cracks, while the linear interaction between guided waves and a notch will not introduce such nonlinear phenomena. The nonlinear mode conversion at a through-thickness fatigue crack was also investigated. It was found that complex mode conversion phenomena involving in higher Lamb modes will happen during the nonlinear wave damage interactions. For the through-thickness crack case, symmetric incident wave would only convert to symmetric modes,

while antisymmetric incident wave would convert to both symmetric and antisymmetric modes, but in a selective mode and alternating pattern.

For future work, experimental validation and comparison of the proposed contact LISA model should be conducted. The computation of nonlinear scattering coefficients should be carried out. The same principle should be applicable to the simulation of delamination and impact damage in composite structures.

ACKNOWLEDGEMENTS

REFERENCES

[1] H. Sohn, H. J. Lim, M. P. DeSimio, K. Brown and M. Derriso, "Nonlinear ultrasonic wave modulation for online fatige crack detection," *Journal of Sound and Vibration,* vol. 333, no. 5, pp. 1473-1484, 2014.

[2] J.-Y. Kim, L. J. Jacobs and J. Qu, "Experimental characterization of fatigue damage in a nickel-base superalloy using nonlinear ultrasonic waves," *Journal of Acoustical Society of America,* vol. 120, no. 3, pp. 1266-1273, 2006.

[3] Z. Su, C. Zhou, M. Hong, L. Cheng, Q. Wang and X. Qing, "Acousto-ultrasonics-based fatigue damage characterization: linear versus nonlinear signal features," *Mechanical Systems and Signal Processing,* vol. 45, no. 1, pp. 225-239, 2014.

[4] K.-Y. Jhang, "Nonlinear Ultrasonic Techniques for Nondestructive Assessment of Micro Damage in Material: A Review," *International Journal of Precision Engineering and Manufacturing,* vol. 10, no. 1, pp. 123-135, 2009.

[5] D. Dutta, H. Sohn, K. A. Harries and P. Rizzo, "A nonlinear acoustic technique for crack detection in metallic structures," *Strctural Health Monitoring, An International Journal,* vol. 8, no. 3, pp. 251-262, 2009.

[6] Y. Shen and V. Giurgiutiu, "WaveFormRevealer: An analytical framework and predictive tool for the simulation of multi-modal guided wave propagation and interaction with damage," *Structural Health Monitoring: An International Journal,* vol. 13, no. 5, pp. 491-511, 2014.

[7] Y. Shen and V. Giurgiutiu, "Predictive modeling of nonlinear wave propagation for structural health monitoring with piezoelectric wafer active sensors," *Journal of Intelligent Material Systems and Structures,* vol. 25, no. 4, pp. 506-520, 2013.

[8] S. Hirose, "2-D Scattering by a crack with contact-boundary conditions," *Wave Motion,* vol. 19, no. 1, pp. 37-49, 1994.

[9] K. Yamanaka, Y. Ohara, M. Oguma and Y. Shintaku, "Tow-dimensional analyses of subharmonic generation at closed cracks in nonlinear ultrasonics," *Applied Physics Express,* vol. 4, no. 7, pp. 1-3, 2011.

[10] P. Delsanto, T. Whitcombe, H. Chaskelis and R. Mignogna, "Connection machine simulation of ultrasonic wave propagation in materials. I: The one-dimensional case," *Wave Motion,* vol. 16, no. 1, pp. 65-80, 1992.

[11] P. Delsanto, R. Schechter, H. Chaskelis, R. Mignogna and R. Kline, "Connection machine simulation of ultrasonic wave propagation in materials. II: The two-dimensional case," *Wave Motion,* vol. 20, no. 4, pp. 295-314, 1994.

[12] P. Delsanto, R. Schechter and R. Mignogna, "Connection machine simulation of ultrasonic wave propagation in materials III: The three-dimensional case," *Wave Motion,* vol. 26, no. 4, pp. 329-339, 1997.

[13] K. Nadella and C.E.S. Cesnik, "Numerical simulation of wave propagation in composite plates," in *SPIE Smart Structures and NDE*, San Diego, 2012.

[14] K. Nadella and C.E.S. Cesnik, "Local interaction simulation approach for modeling wave propagation in composite structures," *CEAS Aeronautical Journal,* vol. 4, no. 1, pp. 35-48, 2013.

[15] K. Nadella and C.E.S. Cesnik, "Effect of piezoelectric actuator modeling for wave generation in LISA," in *SPIE Smart structures and NDE*, San Diego, 2014.

[16] M. Obenchain, K. Nadella and C.E.S. Cesnik, "Hybrid global matrix/local interaciton simulation approach for wave proapgation in composites," *AIAA Journal,* vol. 53, no. 2, pp. 379-393, 2014.

[17] Y. Shen and C.E.S. Carlos, "Hybrid local FEM/global LISA modeling of guided wave propagation and interaction with damage in composite structures," in *Proc. SPIE 9438, Health Monitoring of Structural and Biological Systems 2015, 94380J*, San Diego, 2015.

[18] P. Packo, T. Bielak, A. B. Spencer, T. Uhl, W. J. Staszewski, K. Worden, T. Barszcz, P. Russek and K. Wiatr, "Numerical simulations of elastic wave propagation using graphical processing units -- Comparative study of high-performance computing capabilities," *Computer methods in applied mechanics and engineering,* vol. 290, no. 1, pp. 98-126, 2015.

[19] M. Scalerandi, V. Agostini, P. P. Delsanto, K. V. D. Abeele and P. A. Johnson, "Local interaction simulation approach to modelling nonclassical, nonlinear elastic behavior in solids," *Journal of Acoustical Society of America,* vol. 113, no. 6, pp. 3049-3059, 2003.

[20] P. Delsanto, A. Gliozzi, M. Hirsekorn and M. Nobili, "A 2D spring model for the simulation of ultrasonic wave propagation in nonlinear hysteretic media," *Ultrasonics,* vol. 44, no. 3, pp. 279-286, 2006.

[21] M. Scalerandi and V. Agostini, "Simulation of the Propagation of Ultrasonic Pulses in Nonlinear and/or Attenuative Media," *Journal of Computational Acoustics,* vol. 10, no. 3, pp. 275-294, 2002.

[22] M. B. Obenchain and C.E.S. Cesnik, "Guided wave interaction with hole damage using the local interaction simulation approach," *Smart Materials and Structures,* vol. 23, no. 12, pp. 1-14, 2014.